Medical Engineering and Physics 68 (2019) 85–93

Contents lists available at ScienceDirect

Medical Engineering and Physics

journal homepage: www.elsevier.com/locate/medengphy

Phenomenological tissue fracture modeling for an Endoscopic Sinus and Skull Base Surgery training system based on experimental data

Soroush Sadeghnejad[a], Farzam Farahmand[a], Gholamreza Vossoughi[a,*], Hamed Moradi[a], S. Mousa Sadr Hosseini[b]

[a] Mechanical Engineering Department, Sharif University of Technology, Tehran, Iran
[b] School of Medicine, Tehran University of Medical Sciences, Tehran, Iran

ARTICLE INFO

Article history:
Received 13 November 2017
Revised 16 January 2019
Accepted 11 February 2019

Keywords:
ESSS training simulator
Phenomenological model
Fracture force
Sino-nasal tissue
Deformation
Cutting
Kelvin–Voigt model
Rate dependency

ABSTRACT

The ideal simulator for Endoscopic Sinus and Skull Base Surgery (ESSS) training must be supported by a physical model and provide repetitive behavior in a controlled environment. Development of realistic tissue models is a key part of ESSS virtual reality (VR)-based surgical simulation. Considerable research has been conducted to address haptic or force feedback and propose a phenomenological tissue fracture model for sino-nasal tissue during surgical tool indentation. Mechanical properties of specific sino-nasal regions of the sheep head have been studied in various indentation and relaxation experiments. Tool insertion at different indentation rates into coronal orbital floor (COF) tissue is modeled as a sequence of three events: deformation, fracture, and cutting. The behavior in the deformation phase can be characterized using a non-linear, rate-dependent modified Kelvin–Voigt model. A non-linear model for tissue behavior prior to the fracture point is presented. The overall model shows a non-positive dependency of maximum force on tool indentation rate, which indicates faster tool insertion velocity decreases the maximum final fracture force. The tissue cutting phase has been modeled to characterize the force necessary to slice through the COF. The proposed model in this study can help develop VR-based ESSS base simulators in otolaryngology and ophthalmology surgeries. Such simulators are useful in preoperative planning, accurate surgical simulation, intelligent robotic assistance, and treatment applications.

1. Introduction

Endoscopic Sinus and Skull Base Surgery (ESSS) is a valuable technique in ear, nose and throat (ENT) medicine [1]. However, proficiency in paranasal sinuses and anterior skull base surgery is required by surgeons, residents, and medical students. With increasing complexity of endoscopic tools and procedures and increasing demand to learn anatomy, physiology of the sinus tissues and improve surgical skills, ESSS training seems to be vital. ESSS training simulators have therefore been developed for effective residency training [2]. The ideal simulator for ESSS training must be supported by a physical model [3,4] and provide repetitive behavior in a controlled environment [5]. Such models should represent both the instruments and the related anatomical structures and realistically render the interaction of tools with a variety of soft, semi-soft, and rigid tissues [6,7]. Development of ESSS simulators for a clinical environment depends on a thorough understanding of tool–tissue interaction mechanics [8]. The lack of data in the literature on behavior of soft and hard tissues in sinus and nasal cavity environments and tissue behavior during the fracture/rupture phases has significantly hindered development of virtual reality (VR)-based ESSS simulators.

During ESSS, particularly when the surgeon attempts to remove some endonasal walls of sinus areas to reach a specific region (e.g., a tumor position), transitions between tissue layers often lead to fracture of different walls and organs. The resulting large deformation and forces exerted on the surgical instruments give rise to excessive position errors for a robotic system operating in the sino-nasal cavity. The consequence of such a transition is the position errors for a robotic system operating in the sino-nasal organs. In an effort to provide the surgeons with realistic haptic or force feedback when using surgical training systems, considerable research effort has been devoted to the development of detailed force interaction models [9,10]. Recently, there has been wide interest in tool–tissue interaction force modeling without considering the fracture phase. These models, which are based on Finite-element [11,12], empirical [13,14] and analytical models [15,16], apply for the most part to soft tissues.

Several pioneering reports on the use of force models of needle steering into the soft tissues have appeared recently [17,18]. Mahvash et al. [19] studied the mechanics of needle steering into

* Corresponding author.
E-mail address: vossough@sharif.edu (G. Vossoughi).

https://doi.org/10.1016/j.medengphy.2019.02.004
1350-4533/

biological material based on mechanical fracture methods. While the proposed methodology was interesting, there is as yet no complete model for predicting tissue behavior prior and subsequent to the fracture point. Most studies have involved abdominal tissues during laparoscopic minimally invasive surgery (MIS) [20,21]. Few studies of ESSS procedures have considered hard rate-dependent properties of sino-nasal tissues.

The current research addresses the interactions between surgical tools and non-homogeneous tissues comprising soft and hard tissues, followed by fracture. The characterization of these interactions remains a complex task. For example, as the ESSS tool penetrates the tissues, it crosses different layers composed of both soft and hard tissues and the mechanical properties of each layer are inherently different owing to their inhomogeneity. Furthermore, the value of these parameters may be patient-dependent. When the ESSS tool is inserted into such tissue, the elementary contributions of the different tissue layers are superimposed and/or non-linearly coupled. Also, as the tool pierces the tissues, the interaction is clearly non-linear. With all the aforementioned reasons in mind, haptic models that attempt to define the relationship between motion and interaction forces remain a challenging task in ESSS procedures. Hence efforts are being made to create a phenomenological fracture model for the sino-nasal regions of the sheep head during use of surgical instruments. By performing some indentation and relaxation experimental surveys, the tool insertion process into the sino-nasal tissue is modeled as a sequence of three events: deformation, fracture, and cutting. The effect of indentation rate on force–displacement characteristics during tool insertion is investigated in the present work. We propose a complete model that provides a better sense of tissue fracture during the surgical procedure. The behavior in the deformation phase can be explained using a non-linear, rate-dependent model. We propose a model to predict the behavior of tissue at the fracture point. The model explains why fracture force decreases with increasing insertion rate for some tissue structures. To complete the surveys, we present a non-linear, rate-dependent model for tissue behavior before and after the tissue fracture. Experiments confirm the proposed analytical model in an ovine model of the coronal orbital floor (COF).

2. Methodology, preparation, and experiments

2.1. The methodology of ESSS technical concepts

ESSS involves the insertion of a flexible or rigid fiber-optic tube called an endoscope into the nose for direct visual examination of the openings into the sino-nasal regions. In practice, a specified region is located by inserting a micro-structural instrument like a “Curette” into the rigid walls or cutting the tissues using different instruments. Although this procedure can be performed robotically or even manually, having a deep insight into tissue behavior under various indentation forces is essential to avoid inserting any excessive forces for a safe robotic system or even a VR-based simulator.

2.2. Sino-nasal specimen preparations and experimental set-ups

Given the ethical issues in supplying human cadavers and the low number of cadaver donations in many countries, animal cadaver models are ideal for ESSS training and collection of experimental data for mechanical characterization of sino-nasal tissues [22]. In this research, studies on 15 adult sheep fresh-frozen cadaver specimens were performed for all considered experiments. Sheep heads were purchased fresh from an abattoir. Each head was halved with a saw to ease experimental procedures. All specimens were tested at room temperature. Given the similarity between sino-nasal tissues of sheep and humans, experiments were performed ex-vivo and tool insertions in the sheep sino-nasal region were used as the benchmark.

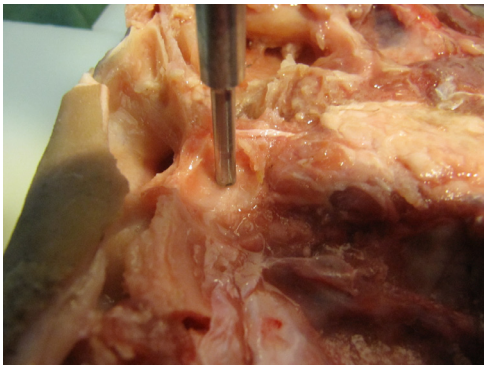

Fig. 1. Indentation and relaxation experimental set-up; an indenter based on the Nasal Surgery Curette instrument.

The two most common types of considered experiment were indentation and relaxation tests. All these experiments were performed using the INSTRON 5560 Series Table Model Testing Systems. To measure the mechanical behavior of the sino-nasal region, we developed an indenter based on the surgery tool (nasal surgery Curette instrument) with a rounded tip of 4 mm diameter. This indenter can be inserted into the various sino-nasal areas and the system records the displacement-force response of the tissue using the piezoelectric load cell attached to the device.

2.3. Anatomical site selection of the sino-nasal region and experimental procedures

An ENT surgeon from Tehran University of Medical Science supervised the animal experiments, provided an insight into sino-nasal anatomy of the sheep head and guided the choice of appropriate regions for further study. The approach was typically the same as actual surgery. To start the main procedures, a point-to-point registration of specimen was necessary to estimate tool and endoscope tip positions in the coordinates of the tracking system. Before acquiring any Computed Tomography (CT) images from the specimen, 8 Acrylonitrile Butadiene Styrene (ABS) landmarks were implanted in the sheep head to give easily recognized images that can be found in the tracking system reference frame for registration purposes, navigation and future data processing. The surgeon stood to the right of the cadaver sheep head, holding the endoscope with his left hand and operating the forceps and curette with his right hand. The goal was to fully open all the sinuses and nasal cavities. Using the tracking system, the surgeon recorded motion data of the endoscope and instruments (Fig. 2). The surgeon could identify and determine the relevant areas during surgery, thus improving safety. Four of the anatomical candidate sites, the COF, skull base, skull rigid wall, and palate, were carefully tested. The COF comprises hard and soft tissues, which protect the eyes and optic nerves, and was selected for further study.

To model tissue fractures in ESSS, an indentation test was performed to characterize the force versus displacement responses of available specimens at rates of 10, 70, 100, 150, 250, and 500 mm/min. Measurements were taken three times for each rate in the various heads, resulting in a total of 18 specimens. Raw displacement and force data collected from different heads are presented in Section 4 as a function of displacement and time. Relaxation tests were also performed to evaluate the mechanical properties of tissues and to model tool–tissue interactions. A position step input was first indented to pre-defined depths of 2, 4, 6 and 8 mm, with the indenter speed of 250 mm/min and held there for the 30 s to record the force relaxation response of

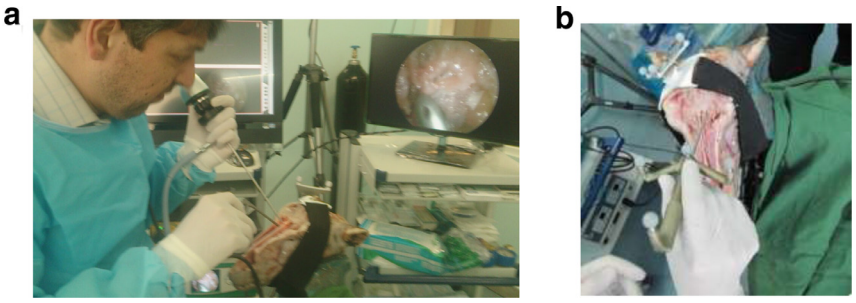

Fig. 2. (a) Sheep sino-nasal anatomy identification, (b) registration procedures.

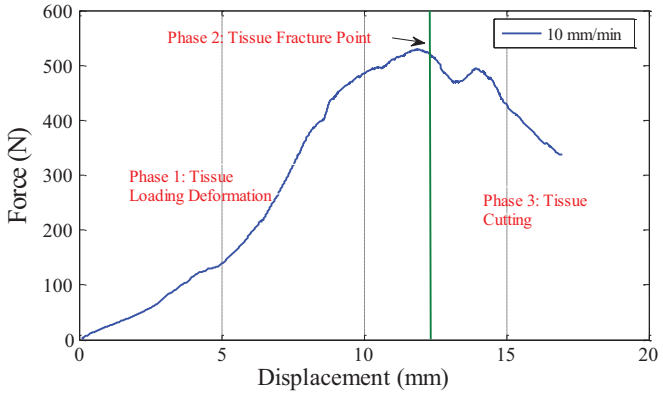

Fig. 3. Measured tool axial force during the interaction with the coronal orbital floor of sheep head.

the tool with respect to time and the exerted forces were measured [23]. Measurements were taken three times for each depth in the various specimens. Hence, a total of four probing measurements were taken in the relaxation experiments from 12 different specimens. Measuring tissue viscoelastic parameters from indentation and relaxation experiments enables fracture phenomena to be easily modeled to study tool–tissue interaction in endoscopic endonasal sinus surgery.

3. Tissue phenomenological model characterization

3.1. Characterization of tool insertion forces

To characterize tool–tissue interaction, force data were separated into components from the sequence of events associated with tool interaction. Models can be developed to predict the relationship between acquired force data, tissue deformation, and velocity. The designed tooltip is assumed to be motionless initially and in contact with the sino-nasal surface. Sample force versus position data acquired during tool insertion into the COF (Fig. 3) reveal one primary fracture and subsequent internal fracture, which is designated by a peak in the force magnitude after a non-linear rise, and a major abrupt linear fall. To summarize this observation, three phenomenological phases can be defined as:

Tissue-loading deformation (Phase 1): the tool pushes the COF surface up to a specific deformation, showing non-linear behavior. This phase corresponds to a non-linear viscoelastic interaction.

Tissue fracture point (Phase 2): when the applied force reaches a definite threshold, the tool penetrates abruptly into the COF by crossing the surface of the tissue.

Tissue cutting (Phase 3): this phase starts right after the force reaches the fracture point and continues by inserting the tool into the damaged tissue.

To characterize a mathematical model that demonstrates the fracture phenomenon requires identification of a general relation

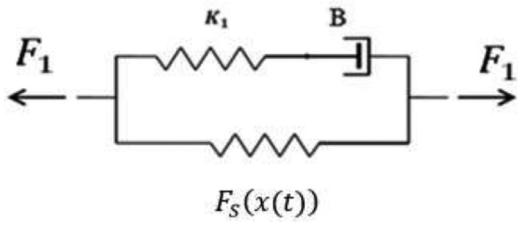

Fig. 4. Modified standard non-linear viscoelastic model (Kelvin–Voigt Model).

between forces and deformation, prior and subsequent to the fracture point. Thus, total forces on the surgical tool can be represented as:

$$F(x,\ \dot{x},\ t) = \begin{cases} F_1(x,\ \dot{x}) & x \le X_f \\ F_2(x,\ \dot{x}) & x > X_f \end{cases},\ X_f(t) = H(\dot{x}) \tag{1}$$

where F_1 is the loading deformation force due to the rate-dependent non-linearity of the organ, identified from pre-fracture forces in the tool–tissue interaction data; and F_2 is the cutting force due to the rate-dependent non-linearity of the tissue, identified after the fracture. X_f, is the condition where the switching of phases occurs. Both the inherent non-linearity of the tissue geometry and the material non-linearity result in the non-linear force-deformation characteristic, as shown in Fig. 3. The separation of these two phases is impossible here because of the limitation of indentation procedures. Also, to develop a realistic model from the acquired data, the specimens are not preconditioned, as is often done in the literature [24]. This means the proposed model can accurately reflect the forces produced during actual interactions.

3.2. Contact model

The classical, standard, non-linear, rate-dependent model is used to predict deformation of tissues before and after fracture. A schematic representation of this standard, non-linear solid model is shown in Fig. 4. To create a phenomenological model, the forces applied by the tool are considered based on the modified Kelvin–Voigt model proposed in [19].

In the proposed model, there are two distinct functions contributing to the total force. The static component of the tool force, which is a non-linear force-deformation function, and the dynamic component of the force, which is presented by a series connection of non-linear springs and dampers. Assuming the standard non-linear viscoelastic model, the contact force can be described as:

$$F_1 = F_S(x(t)) + F_D(x,t) \tag{2}$$

where F_1 is the total force exerted by the tool during any interaction with any tissue, F_S is the non-linear part of the static force, which is explicitly dependent on the deformation ($x(t)$), and F_D is the dynamic component of the exerted force and is dependent on both the tool deformation and time as:

$$F_D(x,t) = K_1 x_K = B\dot{x}_B \tag{3}$$

where the series connection of a spring K_1 and a damper B calculates the dynamic component of the tool–tissue interaction force. x_K is the displacement of the aforementioned spring and x_B is the displacement of the damper, given as:

$$x_B + x_K = x \tag{4}$$

Combination of Eqs. (2)–(4) and assuming that K_1 is constant, yields:

$$F_I(x,t) = F_S(x(t)) + K_I x_K \tag{5}$$

Taking a time derivative of Eq. (5) and using the derivative of Eq. (4) we have:

$$\dot{F}_1 = \dot{F}_S + K_1\left(\dot{x} - \frac{K_1}{B}x_k\right) \tag{6}$$

With regard to Eqs. (2) and (3):

$$\dot{F}_1 = \dot{F}_S + K_1\left(\dot{x} - \frac{F_1 - F_S}{B}\right) \tag{7}$$

Then the general force–displacement relationship is obtained as follows:

$$B\dot{F}_1 + K_1F_1 = B\dot{F}_S + K_1F_s + BK_1\dot{x} \tag{8}$$

Assuming a linear function for the static component, e.g. $F_s = K_2x$, a general representation of the standard linear viscoelastic model can be written as:

$$B\dot{F}_1 + K_1F_1 = K_1K_2x + B(K_1 + K_2)\dot{x} \tag{9}$$

Assuming the relaxation time τ_s is independent of x (due to the dependency of both stiffness and damping parameters to a same function of deformation with the different ratio), different relations can be defined based on the proposed model and basic concept of the modified Kelvin–Voigt model. Using Eq. (3) and defining $\tau_s = B/K_1$, the spring deformation is obtained as:

$$x_K = \tau_s\dot{x}_B \tag{10}$$

Taking the time derivative of Eq. (5) and combining the result with Eq. (10) yields a linear differential equation for spring displacement. The general solution for the aforementioned equation with respect to a constant tool velocity v can be obtained by a convolution integral. Therefore, the total force–deformation response of the model can be expressed as:

$$F_1(x(t)) = F_s(x(t)) + K_1v\tau_s\left(1 - \exp\left(-\frac{x}{v\tau_s}\right)\right) \tag{11}$$

Given a deformation, increasing the indentation velocity always increases the tool–tissue interaction force. Also, Eq. (11) reveals that the peak interaction force is a decreasing function of insertion velocity. To evaluate the modified contact model for this phase, the parameters of the modified Kelvin–Voigt model should be identified. Under very low indentation velocity condition, force data are best fitted by a third-order polynomial. Therefore, for the static part, a third-order polynomial function is assumed in the following form:

$$F_s(x(t)) = a_1x + a_2x^2 + a_3x^3 \tag{12}$$

Considering Eq. (4) and taking the time derivative of Eq. (12), yields:

$$\dot{F}_S = \frac{dF_s}{dt} = \dot{x}(a_1 + 2a_2x + 3a_3x^2) = v(a_1 + 2a_2x + 3a_3x^2) \tag{13}$$

In the offline parameter estimation methods, it is more realistic to calculate the derivative of the force F_1 with respect to displacement x rather than time t, $\dot{F}$ could be rewritten as follows:

$$\dot{F}_1 = \frac{dF_1}{dt} = \frac{dF_1}{dx}\frac{dx}{dt} = v\frac{dF_1}{dx} = vF'_{1x} \tag{14}$$

where, F'_{1x} represents the derivative of the force F_1 with respect to the displacement x. Now, Eq. (8) can be rewritten as follows:

$$F_1 = -\frac{B}{K_1}\dot{F}_1 + \frac{B}{K_1}\dot{F}_S + F_s + B\dot{x} = -\frac{B}{K_1}vF'_{1x} + \frac{B}{K_1}\dot{F}_S + F_s + B\dot{x}$$
$$\dot{x} = v = cte \tag{15}$$

As all the experimental tests have been performed at a constant speed, the velocity v can be treated as a constant coefficient, which leads to:

$$F_1 = -\frac{B}{K_1}vF'_{1x} + \frac{B}{K_1}va_1 + Bv + \left(2\frac{B}{K_1}va_2 + a_1\right)x + \left(3\frac{B}{K_1}va_3 + a_2\right)x^2 + a_3x^3 \tag{16}$$

Therefore, the following general form for the force on the tool in the large deformations can be assumed:

$$F_1 = \theta_1x + \theta_2x^2 + \theta_3x^3 + \theta_4v + \theta_5vx + \theta_6vx^2 - \theta_7vF'_{1x} \tag{17}$$

Eq. (17) can be represented as:

$$F_1 = \varphi^T\theta \tag{18}$$

where

$$\varphi = \begin{bmatrix} x & x^2 & x^3 & v & vx & vx^2 & -vF'_{1x} \end{bmatrix}^T$$

denotes the regression vector and

$$\theta = \begin{bmatrix} \theta_1 & \theta_2 & \theta_3 & \theta_4 & \theta_5 & \theta_6 & \theta_7 \end{bmatrix}^T$$

3.3. Parameter identification for the mechanical model of the tissue

To identify the tissue viscoelastic parameters in Eq. (17), the Sum Square Error (SSE) criterion is used to evaluate the training process. For all general training patterns and model identification outputs, the SSE is calculated by:

$$E(x,\theta) = \frac{1}{2}\sum_{p=1}^{P}\sum_{m=1}^{M_p} {e_{p,m}}^2 \tag{19}$$

In which p is the index of patterns, P is the number of patterns, m is the index of outputs and M_p is the number of outputs in pattern p. x is the input vector, θ is the unknown parameter vector and $e_{p,m}$ is the training error at output m, when applying pattern p and it is defined as

$$e_{p,m} = F_{exp_{p,\,m}} - F_{p,m} \tag{20}$$

where $F_{exp_{p,m}}$ is a force from output m due to pattern p obtained from experimental data and $F_{p,m}$ is the calculated force from the proposed model from the output m due to pattern p. Now, the Jacobian matrix J is introduced as:

$$J = \begin{bmatrix} \frac{\partial e_{1,1}}{\partial\theta_1} & \frac{\partial e_{1,1}}{\partial\theta_2} & \cdots & \frac{\partial e_{1,1}}{\partial\theta_7} \\ \vdots & \vdots & \vdots & \vdots \\ \frac{\partial e_{1,M_1}}{\partial\theta_1} & \frac{\partial e_{1,M_1}}{\partial\theta_2} & \cdots & \frac{\partial e_{1,M_1}}{\partial\theta_7} \\ \vdots & \vdots & \vdots & \vdots \\ \frac{\partial e_{P,M_P}}{\partial\theta_1} & \frac{\partial e_{P,M_P}}{\partial\theta_2} & \cdots & \frac{\partial e_{P,M_P}}{\partial\theta_7} \end{bmatrix}_{(M_1+M_2+\ldots+M_P)\times 7} \tag{21}$$

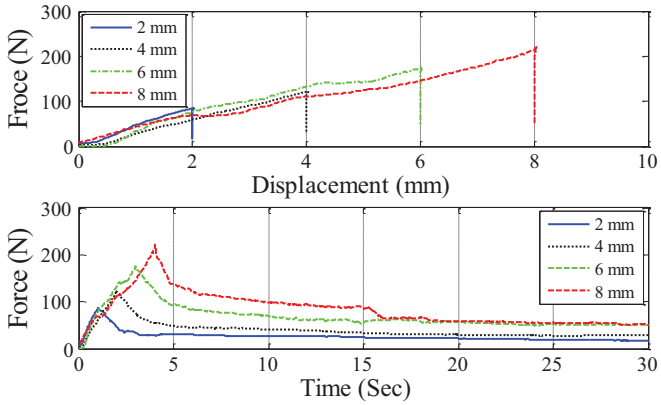

Fig. 5. The force–displacement and force–time curves generated from raw stress relaxation data for the indentation depths of 2, 4, 6 and 8 mm. The indentation rate for all cases was 125 mm/min.

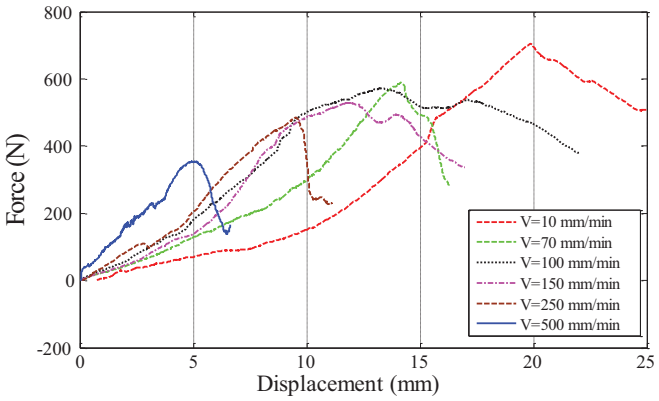

Fig. 6. The complete force–displacement experimental curves for surgical tool insertion into the coronal orbital floor of sheep head with different indentation rates.

where $p = 1, 2, \ldots, P$, in which, the error can be defined as:

$$e = \begin{bmatrix} e_{1,1} \\ \vdots \\ e_{1,M_1} \\ \vdots \\ e_{P,1} \\ \vdots \\ e_{P,M_P} \end{bmatrix}_{(M_1+M_2+\ldots+M_P)\times 1} \tag{22}$$

$$M_p = length\left(\dot{F}_p\right)$$

Considering Eqs. (16) and (20), Eq. (21) can be rewritten in the following new format:

$$J = -\begin{bmatrix} x_{1,1} & {x_{1,1}}^2 & {x_{1,1}}^3 & v_{1,1} & vx_{1,1} & v{x_{1,1}}^2 & -(v\dot{F}_{1x})_{1,1} \\ x_{1,2} & {x_{1,2}}^2 & {x_{1,2}}^3 & v_{1,2} & vx_{1,2} & v{x_{1,2}}^2 & -(v\dot{F}_{1x})_{1,2} \\ \vdots & \vdots & \vdots & \vdots & \vdots & \vdots & \vdots \\ x_{1,M_1} & {x_{1,M_1}}^2 & {x_{1,M_1}}^3 & v_{1,M_1} & vx_{1,M_1} & v{x_{1,M_1}}^2 & -(v\dot{F}_{1x})_{1,M_1} \\ \vdots & \vdots & \vdots & \vdots & \vdots & \vdots & \vdots \\ \vdots & \vdots & \vdots & \vdots & \vdots & \vdots & \vdots \\ \vdots & \vdots & \vdots & \vdots & \vdots & \vdots & \vdots \\ x_{P,1} & {x_{P,1}}^2 & {x_{P,1}}^3 & v_{P,1} & vx_{P,1} & v{x_{P,1}}^2 & -(v\dot{F}_{1x})_{P,1} \\ \vdots & \vdots & \vdots & \vdots & \vdots & \vdots & \vdots \\ x_{P,M_P} & {x_{P,M_P}}^2 & {x_{P,M_P}}^3 & v_{P,M_P} & vx_{P,M_P} & v{x_{P,M_P}}^2 & -(v\dot{F}_{1x})_{P,M_P} \end{bmatrix}_{(M_1+M_2+\ldots+M_P)*7} \tag{23}$$

To minimize the SSE (as defined by Eq. (19)), the iterative method update rule based on the Levenberg–Marquardt algorithm [25] is used, as follows:

$$\theta_{k+1} = \theta_k - \left({J_k}^T J_k + \mu\, I\right)^{-1} {J_k}^T e_k \tag{24}$$

For sufficiently large values of μ, the matrix $({J_k}^T J_k + \mu\, I)$ is positive definite, and a descent direction is guaranteed.

4. Results and validations

4.1. Parameter characterization in the force-deformation model

Four probing measurements of the COF taken from 12 different specimens and four samples of the raw relaxation test data are shown in Fig. 5. After insertion of the tool to the specified depth and prior to the fracture, the tool was instantly stopped to approximate a step change in velocity. When the tool stops, the tissue relaxes and the tool force starts to decrease. As shown in Fig. 5, the force response of COF regions shows more variation and non-linearity as the indentation depth increases. The indentation tests were performed on nine specimens at different rates.

Fig. 6 displays the force–displacement response of the surgical tool insertion into the COF for various indentation rates.

Sino-nasal tissues behave anisotropically as they comprise both hard and soft tissues of non-homogeneous composition. The force response of the tissue shows a stiffening non-linear characteristic with a peak force magnitude depending on the indentation rate. In contrast to hard tissues, sino-nasal tissues may undergo large deformations and also show viscoelastic behavior (relaxation and/or creep). In the absence of large indentation forces, the different layers beneath the surface stay in the relaxed condition and uncompressed tissues behave almost isotropically. As the applied force increases, the different sino-nasal tissue layers start to become loaded: as exerted indentation force increases, the overall deformation also increases. At greater applied forces, the thin, soft mucosal membrane tissue (which covers the harder cartilage and bone tissue) does not deform further, and the harder cartilage and bone tissues start to accommodate the loads. Due to the higher stiffness of such hard tissues, the sino-nasal force–displacement characteristic becomes linear again. In addition, the force–displacement response of the COF shows a stiffer behavior and increased non-linearity prior to the fracture point as the indentation rate decreases. There are three main results based on the experimental data presented in Fig. 6. First, the force required to initiate fracture inversely decreases with tool indentation rate. Second, as the tool penetrates into the COF and passes through different tissues, tissue stiffness starts to decrease after the fracture. This

Table 1
Relaxation time constant parameters.

Test	Indentation depth (mm)	Max force (N)	Relaxation time constant τ_s (s)
1	2	86.64	0.0214
2	4	122.32	0.0212
3	6	176.76	0.0206
4	8	221.37	0.0209

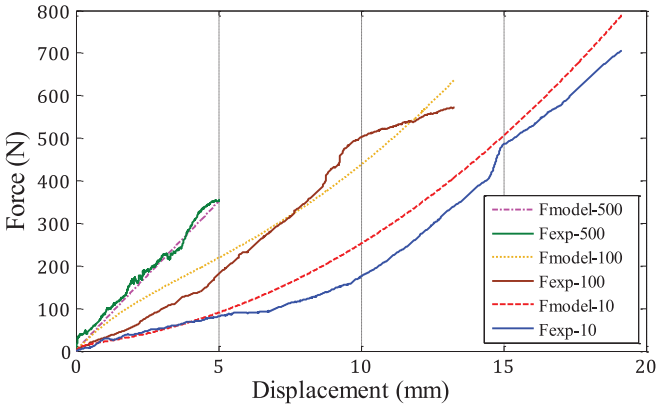

Fig. 7. The force model in tool–tissue interaction compared with the real force signals in three different insertions on real coronal orbital floor regions.

is also expected due to the fracture and break-up of the harder cartilage and bone tissues around the indentation zone. Third, if we consider human subjects with differences in race, sex and age as well as location of indentation on the COF on different specimens, there is significant variability in results [26,27]. Consequently, the peak force corresponding to the fracture point varies among different trials for the same tool indentation rate. The relaxation time τ_s can be determined using the obtained data from the relaxation experiments. Based on the results presented in Fig. 5, an exponential force-time equation is applied to the relaxation data with the specified initial indentation depth and zero initial tool speed. Table 1 gives the relaxation time from four different relaxation experiments. According to the results, the average relaxation time constant for the COF is calculated approximately as $\tau_s = 0.021$s.

To evaluate the modified Kelvin–Voigt model by Eq. (5), the non-linear static and dynamic parts of the exerted force are estimated based on the Levenberg–Marquardt algorithm proposed in [25]. The estimated model parameters were evaluated by direct comparison of typical simulated and real data at constant velocities. Based on the parameter values, $f_s(x) = 0.008x^3 + 2.087x^2 + 8.766x$, $K_1 = 63.62$ and $\tau_s = 0.021$ (and B can be counted as $\tau_s = B/K_1$, respectively), a complete model of the tool–tissue interaction force profile was created and is compared with the experimental data in Fig. 7.

As shown, the model cannot exactly match the experimental data because of the large variability in different specimens and tool interaction with the cartilages and trabecular bones of different densities. However, the overall trend of the model response is similar to the data collected through experiments. To evaluate how well the identified parameters can predict the experimental datasets recorded for each tool insertion at different velocities, the root mean square (RMS) error of the tool force is computed. The root mean square error deviation (RMSD) of an estimator F_{exp} with respect to an estimated parameter F_{Model} is defined as the square root of the mean square error as:

$$RMSD = \sqrt{\frac{\sum \left(F_{\exp i} - F_{model\ i}\right)^2}{n}} \tag{25}$$

where n is the number of different predictions. On the other hand, as forces with respect to displacements were very variable, it was decided to normalize the definition of error. Therefore, the normalized root mean square error (NRMSD) can be defined as:

$$NRMSD = \frac{RMSD}{\hat{F}_{exp}} \tag{26}$$

$\hat{F}_{exp}$ is the obtained estimated analytical forces. Table 2 indicates the percentage of NRMSD of acquired data from experiments with respect to the data from modeling. Accordingly, the NRMSD of obtained data show a variation of 4.23–10.95%.

Table 3 indicates the peak forces corresponding to the fracture point, mean peak forces, and the standard deviations of the data based on 18 measurements for tool insertions into the COF of various specimens. As already predicted, based on the results in Table 3, the average fracture force is a decreasing function of velocity. The largest peak force standard deviation is 52.85 N, which occurs at the test velocity of 10 mm/min and the minimum force standard deviation is 13.19 N, corresponding to the test velocity of 500 mm/min. The standard deviations in other velocities have no meaningful behavior and are an indication of the variability of the mechanical properties of different specimens.

4.2. Parameter characterization of tissue fracture model

To estimate the fracture point of COF and tissue behavior afterwards, a criterion based on the displacement of the tool and its insertion velocity must be established. In the first step, we propose a velocity-based condition for estimating fracture displacement (x_f) and maximum fracture force (F_f). Next, the tissue cutting behavior, which is a relation between the cutting force (F_{post}) and its corresponding displacement (x_{post}), is derived by analyzing the collected data. These data are obtained from the tool displacement related to the maximum forces during the insertion process in different trials. The curve-fitting approach is employed to approximate the tissue behavior at the fracture point and beyond. Fig. 8 depicts how the fracture position (x_f) corresponding to each fracture force (F_f) has been fitted as the second-order polynomial function of insertion velocity.

Results show that tissue deformation at the fracture points is nearly a declining polynomial function of displacement. According to Fig. 8, the parameters of the transitioning function for the sheep head COF fracture point are obtained as:

$$X_f(v) = H(v) = 0.0001v^2 - 0.0575v + 19.21 \tag{27}$$

Table 2
Normalized root mean square error deviation (NRMSD) of experimental data with respect to the data from force modeling prior to fracture.

Velocity	10 (mm/min)	70 (mm/min)	100 (mm/min)	150 (mm/min)	250 (mm/min)	500 (mm/min)
RMSD	0.00297	0.00310	0.00162	0.00182	0.00382	0.00088
NRMSD	0.10953	0.12695	0.07478	0.07771	0.14000	0.04233
%	10.95	12.70	7.48	7.77	14.00	4.23

Table 3
Mean and standard deviation peak/fracture force based on 18 measurements of tool indentation into the coronal orbital floor.

Test	Velocity (mm/min)	Peak force (N) Test 1	Peak force (N) Test 2	Peak force (N) Test 3	Mean peak force (N)	Standard deviation
1	10	709.4802	624.3657	750.6521	694.8327	52.58
2	70	594.8245	572.9675	621.3456	596.3792	19.78
3	100	579.6931	498.3215	609.5362	562.5169	46.99
4	150	534.6637	502.7694	564.6531	534.0385	25.27
5	250	490.5058	421.6532	512.321	474.8267	38.64
6	500	359.0062	346.3388	378.4221	361.2557	13.19

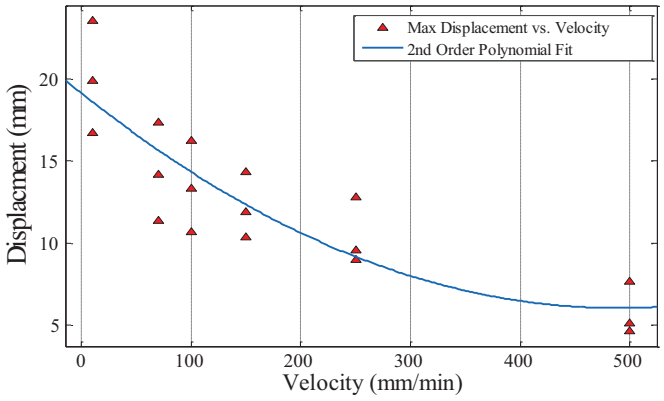

Fig. 8. Second-order polynomial curve fit on obtained experimental fracture displacement (x_f) under different indentation velocities.

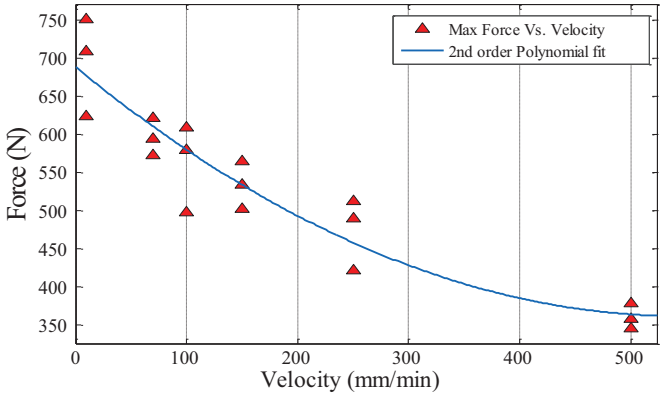

Fig. 9. Second-order polynomial curve fit on obtained experimental fracture forces with different indentation velocities.

4.3. Parametric characterization of tissue cutting model

To have a good insight into the tool insertion velocity effect on fracture forces, the same study presented in Section 4.2 is conducted here. The obtained fracture forces in different trials with various insertion velocities are shown in Fig. 9.

The curve-fitting method is employed to estimate the most appropriate model for the dependency of fracture forces on tool insertion velocities. According to Fig. 9, parameters of COF fracture forces with respect to tool insertion velocity are obtained as:

$$F_f = G(v) = 0.001v^2 - 1.176v + 697.1 \tag{28}$$

The experiments demonstrate that average maximum force is a descending function of velocity, as already predicted by Eq. (11). The tissue cutting behavior can be specified by studying the obtained force-deformation data from the conducted experiments. The cutting force is necessary for the tooltip to slice through the COF. This force is assumed to be a combination of the cutting forces and tissue stiffness at the tip of the surgery tool, which cannot be easily distinguished in the presented study. As shown in Fig. 6, the tissue force–displacement behavior after the fracture point can be approximated by a linear function with a slope that is a function of tool insertion velocity. Hence, based on the experimental data, we intend to find a linear force function of displacement as in:

$$F_2 = F_{post}(x, v) = F_f(v) + a(v) * \left(x_{post} - x_f(v)\right) \tag{29}$$

F_{post} represents the mechanical model of tissue cutting forces, which is dependent on both tool displacement and velocity. $a(v)$ is the slope of the experimental data, beyond the fracture point, as a function of tool insertion rates. x_{post} is the tool displacement beyond fracture. Taking into account Eqs. (27) and (28), $x_f(v)$ and $F_f(v)$ show the dependency of fracture force as well as displacement to the tool indentation rate. Moreover, $a(v)$ shows the dependency of tissue force–displacement slope beyond the tissue fracture (Fig. 9).

Using the same approach, a polynomial-fitted model was used to relate the slopes of force–displacement curves for the post-fracture behavior investigation. After examining different Polynomial models, a fourth-order polynomial is adjusted as the best fit:

$$a(v) = a_4v^4 + a_3v^3 + a_2v^2 + a_1v + a_0 \tag{30}$$

The intercept is non-zero because the force is non-zero at the fracture point. Given the collected data from experiments, the parameters are provided as $a_4 = 10^{-7}$, $a_3 = -7 \times 10^{-5}$, $a_2 = 0.0101$, $a_1 = 0.0485$, and $a_0 = -79.313$. Although the NRMSD of obtained data from the non-linear post-fracture model shows a variation of 0.61–14.29% in various trials, the overall linear post-fracture model for a constant tool insertion rate can effectively predict the main cutting phase. Table 4 indicates the percentage of NRMSD of acquired data from experiments with respect to the data obtained from modeling.

4.4. Complete force model of tissue

A complete model for the tool insertion force profile can be established based on the average value of the parameters obtained from the previous sections. The effectiveness of the proposed model has been justified through a series of experiments. The model behavior and experimental data of real simulated surgery tool insertions are compared in Fig. 10.

Although significant variations in sino-nasal geometrical and mechanical properties of any sheep head make it impossible to reach an impeccable match, the overall trend of the proposed model shows an acceptable behavior compared to the experimental data. The major drawback of this method is that the two phases before and after the fracture have been estimated separately. However, this phenomenon induces an additional peak and stiffness force in the data, which reflects the transition across the fracture and the resulting sudden drop of forces following fracture. Despite the limitations of the variation in specimens and the un-modeled parameters, the proposed model may still be used in an ESSS training system and haptic simulations.

Table 4
Normalized root mean square error deviation (NRMSD) of post-fracture data with respect to the model.

Velocity	10 (mm/min)	70 (mm/min)	100 (mm/min)	150 (mm/min)	250 (mm/min)	500 (mm/min)
RMSD	0.00152	0.00202	0.00054	0.00170	0.00042	0.00596
NRSMD	0.01753	0.03069	0.01286	0.02870	0.00614	0.14292
%	1.75	3.07	1.29	2.87	0.61	14.29

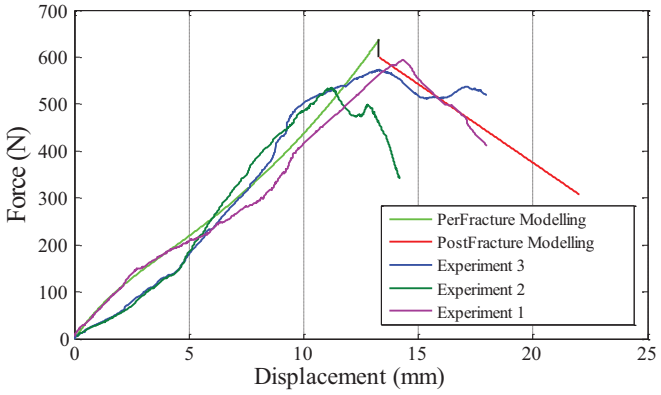

Fig. 10. The tool–tissue interaction model compared with three different insertions with an indentation rate of 100 mm/min on real coronal orbital floor regions.

5. Conclusion and future works

This paper presents methodologies for measurement of stiffness, fracture, and cutting forces, and the effects of tool insertion rate during insertion of the simulated surgery tool into sino-nasal tissues. A qualitative dynamic model is used to express the tool–tissue insertion force prior to fracture of the COF of the sino-nasal region in an ESSS. Performing the ex-vivo tool insertion experiments, we implemented a modified Kelvin–Voigt model to relate force of interaction to tissue deformation. Summarizing the main characteristics of the proposed model, we conclude that the overall model shows a non-positive dependency of maximum force on tool insertion velocity, which means employing a faster tool insertion velocity will decrease the maximum acquired force or the final fracture force. The overall trend of the model behavior is similar to the data collected through experiments in which the approximate tissue fracture point was used to characterize the transition from pre- to post-fracture region of the COF. Finally, the tissue cutting phase has been modeled to characterize the force required for the tooltip to slice through the COF. The accuracy of the proposed approach has been validated to determine the overall complete sino-nasal tissue fracture model during tool insertion into the COF. It is likely that the most comprehensive models require a combination of phenomenological modeling techniques and to be supported by experiments to extract particular force-deformation models. Despite these modeling deviations, the proposed model may still be used for haptic event simulations.

Conflict of interest statement

The authors confirm that this manuscript and its corresponding research work involves no conflict of interest.

Acknowledgment

We are grateful to the Djavad Mowafaghian Research Center of Intelligent Neurorehabilitation Technologies and the Research Center of Biomedical Technology and Robotics at the Research Institute of Medical Technology of Tehran University of Medical Sciences for supporting this research and conducting the experiments. In addition, we would like to thank Farshad Khadivar, Ehsan Abdollahi and Mojtaba Esfandiari for helping us prepare the specimens and set-up system and their helpful comment on several other issues.

Funding

None.

Ethical approval

Not required.

Supplementary materials

Supplementary material associated with this article can be found, in the online version, at doi:10.1016/j.medengphy.2019.02.004.

References

[1] Schneider JS, Burgner J, Webster RJ III, Russell PT III. Robotic surgery for the sinuses and skull base: what are the possibilities and what are the obstacles? Curr Opin Otolaryngol Head Neck Surg 2013;21:11.
[2] Fried MP, Uribe JI, Sadoughi B. The role of virtual reality in surgical training in otorhinolaryngology. Curr Opin Otolaryngol Head Neck Surg 2007;15:163–9.
[3] Sadeghnejad S, Esfandiari M, Farahmand F, Vossoughi G. Phenomenological contact model characterization and haptic simulation of an endoscopic sinus and skull base surgery virtual system. In: Proceedings of the 2016 fourth international conference on robotics and mechatronics (ICROM). IEEE; 2016. p. 84–9.
[4] Rama RR, Skatulla S. Towards real-time cardiac mechanics modelling with patient-specific heart anatomies. Comput Methods Appl Mech Eng; 2017.
[5] Piromchai P. Virtual reality surgical training in ear, nose and throat surgery. Int J Clin Med 2014;05(10):558–66.
[6] Kolbari H, Sadeghnejad S, Bahrami M, Kamali EA. Nonlinear adaptive control for teleoperation systems transitioning between soft and hard tissues. In: Proceedings of the 2015 third RSI international conference on robotics and mechatronics (ICROM). IEEE; 2015. p. 55–60.
[7] Kolbari H, Sadeghnejad S, Bahrami M, Ali KE. Adaptive control of a robot-assisted tele-surgery in interaction with hybrid tissues. J Dyn Syst Meas Control 2018;140(12).
[8] Ariza-Gracia MÁ, Redondo S, Llorens DP, Calvo B, Matas JFR. A predictive tool for determining patient-specific mechanical properties of human corneal tissue. Comput Method Appl Mech Eng 2017;317:226–47.
[9] Kolbari H, Sadeghnejad S, Bahrami M, Kamali A. Bilateral adaptive control of a teleoperation system based on the hunt-crossley dynamic model. In: Proceedings of the 2015 third RSI international conference on robotics and mechatronics (ICROM). IEEE; 2015. p. 651–6.
[10] Ebrahimi A, Sadeghnejad S, Vossoughi G, Moradi H, Farahmand F. Nonlinear adaptive impedance control of virtual tool-tissue interaction for use in endoscopic sinus surgery simulation system. In: Proceedings of the 2016 fourth international conference on robotics and mechatronics (ICROM). IEEE; 2016. p. 66–71.
[11] Tricerri P, Dedè L, Gambaruto A, Quarteroni A, Sequeira A. A numerical study of isotropic and anisotropic constitutive models with relevance to healthy and unhealthy cerebral arterial tissues. Int J Eng Sci 2016;101:126–55.
[12] Tagliabue S, Rossi E, Baino F, Vitale-Brovarone C, Gastaldi D, Vena P. Micro-CT based finite element models for elastic properties of glass–ceramic scaffolds. J Mech Behav Biomed Mater 2017;65:248–55.
[13] Oden JT, Prudencio EE, Hawkins-Daarud A. Selection and assessment of phenomenological models of tumor growth. Math Models Methods Appl Sci 2013;23:1309–38.
[14] Kuhlmann M, Fear E, Ramirez-Serrano A, Federico S. Mechanical model of the breast for the prediction of deformation during imaging. Med Eng Phys 2013;35:470–8.

[15] Suzuki R, Ito K, Lee T, Ogihara N. Parameter identification of hyperelastic material properties of the heel pad based on an analytical contact mechanics model of a spherical indentation. J Mech Behav Biomed Mater 2017;65:753–60.
[16] Safadi M, Rubin M. A new approach to modeling early cardiac morphogenesis during c-looping. Int J Eng Sci 2017;117:1–19.
[17] Bircher K, Ehret AE, Mazza E. Mechanical Characteristics of bovine Glisson's capsule as a model tissue for soft collagenous membranes. J Biomech Eng 2016;138:081005.
[18] de Jong TL, Pluymen LH, van Gerwen DJ, Kleinrensink G-J, Dankelman J, van den Dobbelsteen JJ. PVA matches human liver in needle-tissue interaction. J Mech Behav Biomed Mater 2017;69:223–8.
[19] Mahvash M, Dupont PE. Mechanics of dynamic needle insertion into a biological material. IEEE Trans Biomed Eng 2010;57:934–43.
[20] Fu Y, Chui C. Modelling and simulation of porcine liver tissue indentation using finite element method and uniaxial stress–strain data. J Biomech 2014;47:2430–5.
[21] Cheng L, Hannaford B. Evaluation of liver tissue damage and grasp stability using finite element analysis. Comput Methods Biomech Biomed Eng 2016;19(1):31–40.
[22] Acar B, Gunbey E, Bababemez MA, Karabulut H, Gunbey HP, Karasen RM. Utilization and dissection for endoscopic sinus surgery training in the residency program. J Craniofac Surg 2010;21:1715–18.
[23] Samur E, Sedef M, Basdogan C, Avtan L, Duzgun O. A robotic indenter for minimally invasive measurement and characterization of soft tissue response. Med Image Anal 2007;11:361–73.
[24] Fung Y-C. Biomechanics: mechanical properties of living tissues. Springer Science & Business Media; 2013.
[25] Moré JJ. The Levenberg–Marquardt algorithm: implementation and theory. Numer Anal 1978:105–16.
[26] Evans FG. Mechanical properties of bone: Charles c. Thomas Publisher; 1973.
[27] Al-Sukhun J, Lindqvist C, Kontio R. Modelling of orbital deformation using finite-element analysis. J R Soc Interface 2006;3:255–62.